Angle-resolved photoemission spectroscopy from first-principles quantum Monte Carlo

Cite as: J. Chem. Phys. **149**, 154102 (2018); https://doi.org/10.1063/1.5038864
Submitted: 06 May 2018 . Accepted: 27 September 2018 . Published Online: 15 October 2018

Matteo Barborini, Sandro Sorella, Massimo Rontani, and Stefano Corni

Angle-resolved photoemission spectroscopy from first-principles quantum Monte Carlo

Matteo Barborini,[1,a)] Sandro Sorella,[2] Massimo Rontani,[1] and Stefano Corni[1,3,b)]
[1]*CNR-NANO, Via Campi 213/a, 41125 Modena, Italy*
[2]*Scuola Internazionale Superiore di Studi Avanzati (SISSA) and CNR-IOM Democritos National Simulation Center, Via Bonomea 265, 34136 Trieste, Italy*
[3]*Dipartimento di Scienze Chimiche—Università degli Studi di Padova, Via Marzolo 1, 35131 Padova, Italy*

(Received 6 May 2018; accepted 27 September 2018; published online 15 October 2018)

Angle-resolved photoemission spectroscopy allows one to visualize in momentum space the probability weight maps of electrons subtracted from molecules deposited on a substrate. The interpretation of these maps usually relies on the plane wave approximation through the Fourier transform of single particle orbitals obtained from density functional theory. Here we propose a first-principle many-body approach based on quantum Monte Carlo (QMC) to directly calculate the quasi-particle wave functions (also known as Dyson orbitals) of molecules in momentum space. The comparison between these correlated QMC images and their single particle counterpart highlights features that arise from many-body effects. We test the QMC approach on the linear C_2H_2, CO_2, and N_2 molecules, for which only small amplitude remodulations are visible. Then, we consider the case of the pentacene molecule, focusing on the relationship between the momentum space features and the real space quasi-particle orbital. Eventually, we verify the correlation effects present in the metal $CuCl_4^{2-}$ planar complex. *Published by AIP Publishing.* https://doi.org/10.1063/1.5038864

I. INTRODUCTION

Angle resolved photoemission spectroscopy (ARPES)[1–17] is the main tool to measure electron density maps directly in momentum space. In the last few years, it has also been applied to the tomography of the orbitals of molecules deposited on substrates.[2,8,9,18–21] In ARPES, the photoelectrons are analyzed as a function of their energy and total momentum and their signal is associated with the Fourier transform (FT) of electronic orbitals. This process can be modeled within the plane wave approximation:[2,20,22,23] the probability of the electron to be photodissociated with a certain momentum and energy is linked to the modulus of the Fourier transform of the quasiparticle wave function (QPWF or Dyson orbital[24–28]) of the hole that is created in the process[20] (*h*QPWF). The *h*QPWF may be thought of as the orbital of an electron dressed by the interaction with the other electrons in the molecule as its square modulus is associated with the probability density of removing that electron from the molecule.[26,27,29] In this work, we will limit ourselves to the study of the dissociation processes that leave the ionized molecule in its ground state.

The interpretation of ARPES momentum maps typically relies on the comparison with the Fourier transform (FT) of single particle orbitals from density functional theory (DFT) calculations.[2,6,12,19,30–34] Two important effects are usually disregarded and will also not be considered in this investigation. The first is that of the interaction between the molecule and the substrate on which it is deposited, which has been shown to deeply affect the orbital images:[35,36] The second is related to the fact that for low energy photons, the emitted electron cannot be considered as a free particle and the plane-wave approximation fails, leading to the necessity to account for semi bounded states through time-dependent density-functional[37,38] or Coulomb-wave functions.[39–41] Still, within these approximations, the adequacy of single-particle approaches such as DFT has also been previously questioned and investigated.[20,42]

The main source of error in DFT as pointed out by Perdew and Zunger is due to self-interaction;[43] as a matter of fact, self-interaction-free Kohn-Sham (KS) DFT functionals have been found to be quite successful in interpreting orbital tomography,[20,44,45] giving the correct eigenvalue ordering and eigenfunction character. The same can be said for the Koopmans-compliant functionals that have been seen to give excellent agreement with experimental ultraviolet photoemission spectroscopy and orbital tomography.[30] Moreover, it has been shown that generalised KS functionals can also describe quasi-particle bandgaps giving results comparable to GW calculations.[46–50] This said, however, some limitations still remain: first the quasi-particle orbitals are not normalized like the independent particle ones and more importantly the single-particle picture is unable to describe multideterminantal correlation effects that arise in systems with partial orbital degeneracy.[42]

Here we present an alternative approach to directly calculate the QPWF in momentum space through quantum Monte

[a)]Current address: Physics and Materials Science Research Unit, University of Luxembourg, 162a Avenue de la Faïencerie, L-1511 Luxembourg, Luxembourg.
[b)]Author to whom correspondence should be addressed: stefano.corni@unipd.it

Carlo (QMC),[51–53] which follows from the development of the procedure proposed by us[29] to simulate wave function mapping through scanning tunneling microscopy. The advantages of QMC are of two kinds. First, it is possible to easily calculate the QPWFs as overlaps of correlated multideterminantal wave functions. The latter include few-body interaction terms through a Jastrow factor[54,55] and combine Gaussian and Slater type orbitals, making the basis set convergence faster and recovering a high level of electronic correlation. Second, the QMC algorithms such as those used to stochastically optimize the wave functions[56–58] and to optimize the molecular structures[59–62] are easily parallelized, making them efficient for large systems in high-performance computing facilities.

In the following, we will recall the method to evaluate the QPWF in real space of Ref. 29 and describe in detail the approach to evaluate the QPWF in momentum space. Afterwards, we will test this method to reproduce the outcome of photoemission spectroscopy applied to three linear molecules, N_2, C_2H_2, and CO_2, which have been the object of recent tomography experiments in gas phase.[63–65] Eventually we will focus on the photoemission process for the pentacene molecule,[2] whose orbitals have already been mapped through Scanning Tunneling Spectroscopy (STS)[66] and ARPES.[19] We compare the FT of the HOMO with the *h*QPWF in momentum space obtained from QMC and highlight the origin of the (small) discrepancies between the Hartree-Fock (HF) and the B3LYP DFT HOMOs and the QPWFs in real space. Finally we study the metallic $CuCl_4^{2-}$ planar complex, where correlation effects are expected to be larger.[27]

II. ANGLE RESOLVED PHOTOEMISSION SPECTROSCOPY

The photoemission process taking place in ARPES experiments is described through Fermi's Golden rule,

$$\Gamma_{f\leftarrow i} \propto |\langle \Psi_f^{N_e} | \mathbf{A}\cdot\hat{\mathbf{p}} | \Psi_i^{N_e}\rangle|^2 \delta(\mathrm{E}_f^{N_e} - \mathrm{E}_i^{N_e} - \hbar\omega), \qquad (1)$$

as the transition of the electronic ground state $|\Psi_i^{N_e}\rangle$ of a system of N_e electrons to a final state $|\Psi_f^{N_e}\rangle$ induced by the interaction with a laser field, $\hat{H}_{\mathrm{int}} = \mathbf{A}\cdot\hat{\mathbf{p}}$ (in atomic units, the factor $\frac{e}{m_e}$ is equal to 1). The energies involved in the process are the initial and final state energies, $\mathrm{E}_i^{N_e}$ and $\mathrm{E}_f^{N_e}$, and the energy of the absorbed photon, $\hbar\omega$. In the plane wave approximation,[2,22,23] the final state of the molecule plus the detached electron is approximated as the direct product of the ionic molecular ground state times a one-electron plane wave. The plane wave approximates the asymptotic state of the detached electron, which is free from interaction with the remaining electrons in the molecule and unaffected by the Coulomb potential of the positively charged ion. Hence, the transition matrix element reduces to the equation[20,25]

$$\Gamma_{f\leftarrow i} \propto |\mathbf{A}\cdot\mathbf{k}|^2 |\tilde{\varphi}_{h\mathrm{QPWF}}(\mathbf{k})|^2_{|\mathbf{k}|=const.}, \qquad (2)$$

where $\tilde{\varphi}_{h\mathrm{QPWF}}(\mathbf{k})$ is the Fourier transform of the *h*QPWF occupied by the hole created by absorbing the photon and $|\mathbf{k}| = \sqrt{\frac{2m_e}{\hbar^2}\epsilon_k}$ is related to the kinetic energy of the free electron through $\epsilon_k = \hbar\omega + \mathrm{E}_i^{N_e} - \mathrm{E}_f^{N_e-1}$. We recall that the *hole*-quasiparticle wave function is associated with the probability of removing the electron from the ground state of the molecule, which leaves an empty orbital dressed by the interaction between the hole and electrons remaining in the system. Since the term $|\mathbf{A}\cdot\mathbf{k}|^2$ can be factored out in the analysis of the experiment, the ARPES map depends only on the calculated modulus $|\tilde{\varphi}_{h\mathrm{QPWF}}(\mathbf{k})|_{|\mathbf{k}|=\mathrm{const.}}$. As shown in Fig. 1, this corresponds to first Fourier-transforming the *h*QPWF in real space [Fig. 1(a)] and then considering the hemisphere of fixed radius $|\mathbf{k}|$ in reciprocal space [Fig. 1(b)]. In orbital tomography experiments based on ARPES, $|\tilde{\varphi}_{h\mathrm{QPWF}}(\mathbf{k})|_{|\mathbf{k}|=const.}$ is retrieved for different values of the electron energy, providing a three-dimensional mapping of the orbital in momentum space, which is Fourier-transformed in real space, reconstructing the orbital involved in the photoionization process.[19]

A. Quasiparticle wave functions in real space with quantum Monte Carlo

Quantum Monte Carlo (QMC) methods are stochastic techniques used to calculate the mean values of physical observables over certain optimized trial wave functions that approximate the ground or excited states of the electronic systems. To compute a QMC average, the integrand must be rewritten as the product of a probability density times a local quantity of the electronic configurations. Before discussing the procedure to define the *h*QPWF in momentum space, here we briefly recall the method described in Ref. 29 to determine the *h*QPWF in real space. The *h*QPWF is

$$\varphi_{h\mathrm{QPWF}}(\mathbf{r}) = \sqrt{\frac{N_e}{\mathcal{N}_{N_e}\mathcal{N}_{N_e-1}}} \int d\bar{\mathbf{r}}_{(N_e-1)} \Psi_{N_e}(\bar{\mathbf{r}}_{(N_e-1)}, \mathbf{r}) \times \Psi_{N_e-1}(\bar{\mathbf{r}}_{(N_e-1)}), \qquad (3)$$

where the normalization factors of the two many-body wave functions that appear explicitly in the integrand, $\mathcal{N}_{N_e} = \int d\bar{\mathbf{r}}_{(N_e)} |\Psi_{N_e}(\bar{\mathbf{r}}_{(N_e)})|^2$ and $\mathcal{N}_{N_e-1} = \int d\bar{\mathbf{r}}_{(N_e-1)} |\Psi_{N_e-1}(\bar{\mathbf{r}}_{(N_e-1)})|^2$, and $\bar{\mathbf{r}}_{(N_e+1)} = \{\mathbf{r}_1, \ldots, \mathbf{r}_{N_e}, \mathbf{r}_{N_e+1}\}$, $\bar{\mathbf{r}}_{(N_e)} = \{\mathbf{r}_1, \ldots, \mathbf{r}_{N_e}\}$ are the configuration vectors containing the electronic

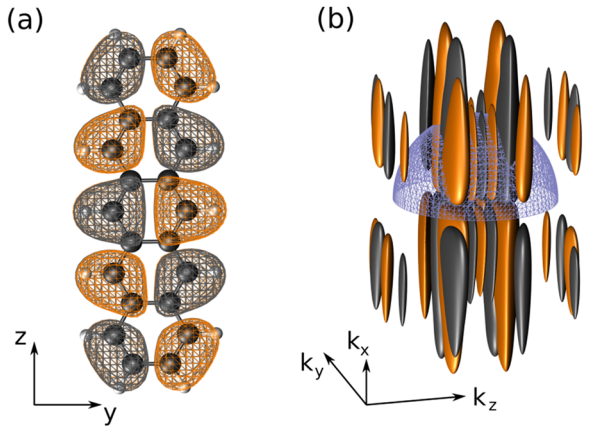

FIG. 1. (a) *h*QPWF of the pentacene molecule. (b) Fourier transform of the *h*QPWF. The blue hemisphere shown in (b) represents the surface with constant $|\mathbf{k}|$ that is reconstructed in ARPES experiments.

coordinates. In order to evaluate Eq. (3), we rewrite the integrand as the product of a local quantity times a probability density related to the square modulus of the stochastically sampled wave function. Assuming we sample the square modulus of the cationic wave function, we accomplish this by multiplying and dividing the integrand by $\Psi_{N_e-1}(\bar{\mathbf{r}}_{(N_e-1)})/\sqrt{\mathcal{N}_{N_e-1}}$, we obtain the integral of the product of two functions

$$\varphi_{h\mathrm{QPWF}}(\mathbf{r}) = \mathcal{Q}\int d\bar{\mathbf{r}}_{(N_e-1)}\frac{\Psi_{N_e}(\bar{\mathbf{r}}_{(N_e-1)},\mathbf{r})}{\Psi_{N_e-1}(\bar{\mathbf{r}}_{(N_e-1)})} \times \Pi_{N_e-1}(\bar{\mathbf{r}}_{(N_e-1)}), \tag{4}$$

which are, respectively, the wave function ratio and the probability density, $\Pi_{N_e-1}(\bar{\mathbf{r}}_{(N_e-1)}) = |\Psi_{N_e-1}(\bar{\mathbf{r}}_{(N_e-1)})|^2/\mathcal{N}_{N_e-1}$, associated with the $\Psi_{N_e-1}(\bar{\mathbf{r}}_{N_e-1})$ many-body wave function. This product is further multiplied by a constant factor, $\mathcal{Q}$, defined as the ratio between the two normalization factors

$$\mathcal{Q} = \sqrt{N_e\frac{\mathcal{N}_{N_e-1}}{\mathcal{N}_{N_e}}}. \tag{5}$$

In this way, the integral (4) is evaluated as the mean value of the ratio $\Psi_{N_e}(\bar{\mathbf{r}}_{(N_e-1)},\mathbf{r})/\Psi_{N_e-1}(\bar{\mathbf{r}}_{(N_e-1)})$ estimated for a certain number of electronic configuration vectors which are stochastically sampled according to the probability $\Pi_{N_e-1}(\bar{\mathbf{r}}_{(N_e-1)})$,

$$\varphi_{h\mathrm{QPWF}}(\mathbf{r}) = \mathcal{Q}\left\langle\frac{\Psi_{N_e}(\bar{\mathbf{r}}_{(N_e-1)},\mathbf{r})}{\Psi_{N_e-1}(\bar{\mathbf{r}}_{(N_e-1)})}\right\rangle_{\Pi_{N_e-1}}. \tag{6}$$

In practice, the Ψ_{N_e-1} wave function that appears in the ratio is calculated on the $\bar{\mathbf{r}}_{(N_e-1)}$ electronic configuration generated during the stochastic sampling, whereas the Ψ_{N_e} is calculated by adding to the N_e-1 electrons another electron in the position $\mathbf{r}$, the same location in which we evaluate the QPWF.

As described in Ref. 29, the square of the prefactor $\mathcal{Q}$ can be evaluated as the ratio

$$\mathcal{Q}^2(\mathbf{r}) = N_e\frac{\left\langle\frac{1}{N_e}\sum_{i=1}^{N_e}\frac{\Psi_{N_e-1}(\mathbf{r}_1,\ldots,\cancel{\mathbf{r}_i},\ldots,\mathbf{r}_{N_e})\delta(\mathbf{r}-\mathbf{r}_i)}{\Psi_{N_e}(\bar{\mathbf{r}}_{(N_e)})}\right\rangle_{\Pi_{N_e}}}{\left\langle\frac{\Psi_{N_e}(\bar{\mathbf{r}}_{(N_e-1)},\mathbf{r})}{\Psi_{N_e-1}(\bar{\mathbf{r}}_{(N_e-1)})}\right\rangle_{\Pi_{N_e-1}}}, \tag{7}$$

where the denominator is the same mean value defined in Eq. (6), while the numerator is evaluated following a similar procedure in which we sample the wave function of the reference molecular ground state with N_e total electrons. Note that the $\Psi_{N_e}(\bar{\mathbf{r}}_{(N_e)})$ function is evaluated on stochastically sampled configurations, while the $\Psi_{N_e-1}(\mathbf{r}_1,\ldots,\cancel{\mathbf{r}_i},\ldots,\mathbf{r}_{N_e})\delta(\mathbf{r}-\mathbf{r}_i)$ is evaluated over this same set of configurations provided we remove the ith electron, according to the condition $\delta(\mathbf{r}-\mathbf{r}_i)$. Of course there are N_e electrons that can be removed in this manner, and this explains the mean value over N_e that appears in the numerator of Eq. (7). Since the probability of finding an electron satisfying the condition $\delta(\mathbf{r}-\mathbf{r}_i)$ when sampling randomly is zero, a practical procedure to evaluate $\mathcal{Q}$ relies on evaluating the ratio of the integrals of the numerator and the denominator on the same finite volume $\mathcal{V}$. Formally, this corresponds to applying two quasiparticle operators that create or delete an electron in a volume $\mathcal{V}$, i.e., $Z^\dagger = \int_{\mathbf{r}\in\mathcal{V}}\psi^\dagger_{\mathbf{r}}d\mathbf{r}$ and $Z = \int_{\mathbf{r}\in\mathcal{V}}\psi_{\mathbf{r}}d\mathbf{r}$. Within this approach, the error of the numerator in $\mathcal{Q}$ is always finite.[29]

B. Quasiparticle wave function in momentum space with quantum Monte Carlo

Following the above procedure, we can calculate the hQPWF in momentum space defined as the FT of the hQPWF [Eq. (3)],

$$\tilde{\varphi}_{h\mathrm{QPWF}}(\mathbf{k}) = \sqrt{\frac{N_e}{\mathcal{N}_{N_e}\mathcal{N}_{N_e-1}}}\int d\mathbf{r}e^{i\mathbf{k}\cdot\mathbf{r}}\int d\bar{\mathbf{r}}_{(N_e-1)} \times\Psi_{N_e}(\bar{\mathbf{r}}_{(N_e-1)},\mathbf{r})\Psi_{N_e-1}(\bar{\mathbf{r}}_{(N_e-1)}), \tag{8}$$

which can be rewritten as

$$\tilde{\varphi}_{h\mathrm{QPWF}}(\mathbf{k}) = \sqrt{\frac{N_e}{\mathcal{N}_{N_e}\mathcal{N}_{N_e-1}}}\int d\bar{\mathbf{r}}_{(N_e)}e^{i\mathbf{k}\cdot\mathbf{r}_{N_e}}\Psi_{N_e}(\bar{\mathbf{r}}_{(N_e)}) \times\Psi_{N_e-1}(\bar{\mathbf{r}}_{(N_e-1)}). \tag{9}$$

To rewrite the integrand as a product of a local function and a probability density, as done for the previous expression in real space, we divide and multiply by the function $\Psi_{N_e}(\bar{\mathbf{r}}_{(N_e)})/\sqrt{\mathcal{N}_{N_e}}$ so that we obtain

$$\tilde{\varphi}_{h\mathrm{QPWF}}(\mathbf{k}) = \frac{N_e}{\mathcal{Q}}\int d\bar{\mathbf{r}}_{(N_e)}\frac{\Psi_{N_e-1}(\bar{\mathbf{r}}_{(N_e-1)})e^{i\mathbf{k}\cdot\mathbf{r}_{N_e}}}{\Psi_{N_e}(\bar{\mathbf{r}}_{(N_e)})}\Pi_{N_e}(\bar{\mathbf{r}}_{(N_e)}), \tag{10}$$

where $\Pi_{N_e}(\bar{\mathbf{r}}_{(N_e)}) = |\Psi_{N_e}(\bar{\mathbf{r}}_{(N_e)})|^2/\mathcal{N}_{N_e}$ is the probability density of extracting the electronic configuration $\bar{\mathbf{r}}_{(N_e)}$. This last expression can be rewritten as the stochastic mean value, similar to that presented in Eq. (6),

$$\tilde{\varphi}_{h\mathrm{QPWF}}(\mathbf{k}) = \frac{N_e}{\mathcal{Q}}\left\langle\frac{\Psi_{N_e-1}(\bar{\mathbf{r}}_{(N_e-1)})e^{i\mathbf{k}\cdot\mathbf{r}_{N_e}}}{\Psi_{N_e}(\bar{\mathbf{r}}_{(N_e)})}\right\rangle_{\Pi_{N_e}}, \tag{11}$$

which can be generalized as the mean value over all the sets of electronic coordinates

$$\tilde{\varphi}_{h\mathrm{QPWF}}(\mathbf{k}) = \frac{1}{\mathcal{Q}}\left\langle\sum_{i=1}^{N_e}\frac{\Psi_{N_e-1}(\mathbf{r}_1\ldots,\cancel{\mathbf{r}_i},\ldots,\mathbf{r}_{N_e})e^{i\mathbf{k}\cdot\mathbf{r}_i}}{\Psi_{N_e}(\bar{\mathbf{r}}_{(N_e)})}\right\rangle_{\Pi_{N_e}}. \tag{12}$$

In practice, the probability Π_{N_e} is sampled by generating a certain number of configurations of N_e electrons. For each configuration, we evaluate the ratio between the function $\Psi_{N_e}(\bar{\mathbf{r}}_{(N_e)})$ and the numerator, where the function $\Psi_{N_e-1}(\mathbf{r}_1\ldots,\cancel{\mathbf{r}_i},\ldots,\mathbf{r}_{N_e})$ is evaluated over the same set of coordinates except we remove the ith electron, its coordinates appearing in the plane wave $e^{i\mathbf{k}\cdot\mathbf{r}_i}$. Equation (12) enables us to calculate directly the hQPWF in momentum space by sampling the probability $|\Pi_{N_e}|^2$ associated with the molecular ground state. Since in ARPES experiments the absolute intensity of the signal is often immaterial, it is not necessary to determine the constant $\mathcal{Q}$. In this work, we evaluate $\mathcal{Q}$ as done in Ref. 29 to compare the total amplitude with the one of the FT of the HOMOs obtained from single particle calculations.

III. COMPUTATIONAL METHODS

A. Variational wave functions

The procedure described above is applied to the correlated wave functions used in quantum Monte Carlo that are built as the product of a fermionic part and a Jastrow factor that includes explicit many-body correlations terms. In this work, we use the Jastrow antisymmetrized geminal power[67,68] (JAGP) wave function already applied to study the structural and electronic properties of various molecular systems,[55,67,69,70] which is able to recover a high level of electronic correlation while remaining relatively compact.[60,71–75]

The fermionic part of the wave function, the antisymmetrized geminal power[76] (AGP), is in fact a constraint multideterminantal expansion that includes various molecular excitations:[55,72,73] this is written as the determinant of geminal functions that explicitly includes the correlation between two electrons in a spin singlet state, as extensively described in Refs. 55, 60, 71–75, and 77–79.

The Jastrow factor[54,55,60] that we use is written as the product of three bosonic terms independent from spin, $J = J_1 J_2 J_{3/4}$, which take into account both nucleus-electron and electron-electron cusp conditions.[54] This factor also includes two-electron correlation terms, a homogeneous one that depends on electron-electron distances and a non-homogeneous one that depends on the relative distances between electrons and nuclei.[55,60,72] These last terms are necessary in order to describe dispersive interactions[70,80] and modulate charge localization.

B. Computational details

The QMC calculations in this work have been performed by means of the TurboRVB[81] code, after implementing a new code routine for the calculation of the quasiparticle wave function in real[29] and momentum space. The wave functions of each molecular species have been fully optimized with the linear method[58,70] with Hessian acceleration.[70] The set of optimized parameters include the coefficients that appear in the AGP matrix and in the Jastrow factor, the coefficients of the contractions of the atomic orbitals, and the exponents of the Gaussian primitives and of the Slater type orbitals. The Hartree-Fock (HF) and density functional theory (DFT) (with PBE, PBE0, and B3LYP functionals) calculations are performed using the Orca package 3.0.3.[82] The structural properties of the linear molecules are taken from the experimental measurements: the R_{CO} = 1.162 Å bond in CO_2 is taken from Ref. 83; the R_{CH} = 1.063 Å and R_{CC} = 1.203 Å bonds in C_2H_2 from Ref. 84 and the R_{NN} = 1.098 Å bond in N_2 from Ref. 85. The ground state structure of pentacene has been optimized with the cc-pVTZ basis set[86] and the B3LYP functional with unrestricted Kohn-Sham orbitals.

In order to test the quality of the QMC basis sets used, a basis set convergence is reported in Table S1 of the supplementary material for the N_2, C_2H_2, and CO_2 molecules, and a full description can be found there. In the following calculations regarding the QPWFs, we have always used the largest of the three basis sets tested, which are summarized in Table I for each atomic species. Although the basis set is still incomplete, the full optimization of the atomic orbitals' parameters enables a faster basis set convergence with respect to other methods in quantum chemistry. This convergence is also fastened by the variational optimization of the three/four body Jastrow factor used to recover dynamical correlation between electron pairs. The basis sets for the determinantal part are built from contracted Gaussian primitives and uncontracted Slater type orbitals, while for the Jastrow factor, we have always used uncontracted Gaussian orbitals.

TABLE I. Basis sets of the CO_2, C_2H_2, N_2, and pentacene molecules.

	AGP basis set	Jastrow basis set
	CO_2, C_2H_2, and N_2 molecules	
H	$(3s1s^*1p1p^*)/[1s1s^*1p^m]$[a]	(2s1p)
C,O,N	$(5s4p2d)/(2s2p1d)+(1s^*1p^*1d^*)$	(3s3p2d)
	Pentacene molecule	
H	(3s2p)/[1s1p]	(2s1p)
C	(5s4p2d)/(2s2p1d)	(3s2p1d)

[a] $1s^*$, $1p^*$, and $1d^*$ orbitals indicate single Slater type orbitals that remain uncontracted in the basis set. The $1p^m$ orbital is built from the contraction of a Gaussian 1p and a Slater type $1p^*$ orbital. All other orbitals are built from contracted or uncontracted Gaussian primitives.

The 1s core electrons of the carbon and nitrogen atoms have been substituted with the relativistic energy consistent pseudopotentials (ECPs) implemented by Burkatzki *et al.* in Ref. 87. The effect of the pseudopotentials on the form of the HOMO orbitals of the N_2, C_2H_2, and CO_2 molecules has been verified through different single particle calculations with HF and DFT (with PBE, PBEh, and B3LYP functionals), comparing the all-electron (AE) calculations with the cc-pVTZ basis set[86] (Fig. S2 of the supplementary material) and with the pseudopotential calculations using the uncontracted VTZ basis set[88] (Fig. S1 of the supplementary material). Only non-significant discrepancies appear in between the AE and ECP calculations, the most visible being related to the N_2 molecule. For consistency, in Secs. IV A–IV C, we always compare single particle ECP calculations with the ECP *h*QPWFs obtained through QMC.

IV. RESULTS AND DISCUSSION

A. The N_2, C_2H_2, and CO_2 molecules

To test our approach, we have first evaluated the *h*QPWF of N_2, C_2H_2, and CO_2 linear molecules in momentum space, which were investigated by orbital tomography experiments based on High Harmonic Generation (HHG) spectroscopy in gas phase.[63–65] Note that the process involved in HHG at first order is the same as in ARPES, with $|\tilde{\varphi}_{h\mathrm{QPWF}}(\mathbf{k})|$ being retrieved as a function of the energy of the photoelectron (that recollides with the molecular ion) and as a function of the angle between the electronic momentum and the molecular axis. First, we have built the *h*QPWFs using the real space approach[29] (Fig. 2). In the left column of Fig. 2, we plot the *h*QPWF along the orbital plane that cuts the molecular axis of, respectively, N_2, C_2H_2, and CO_2. The corresponding maps of the single particle HOMOs obtained from HF and

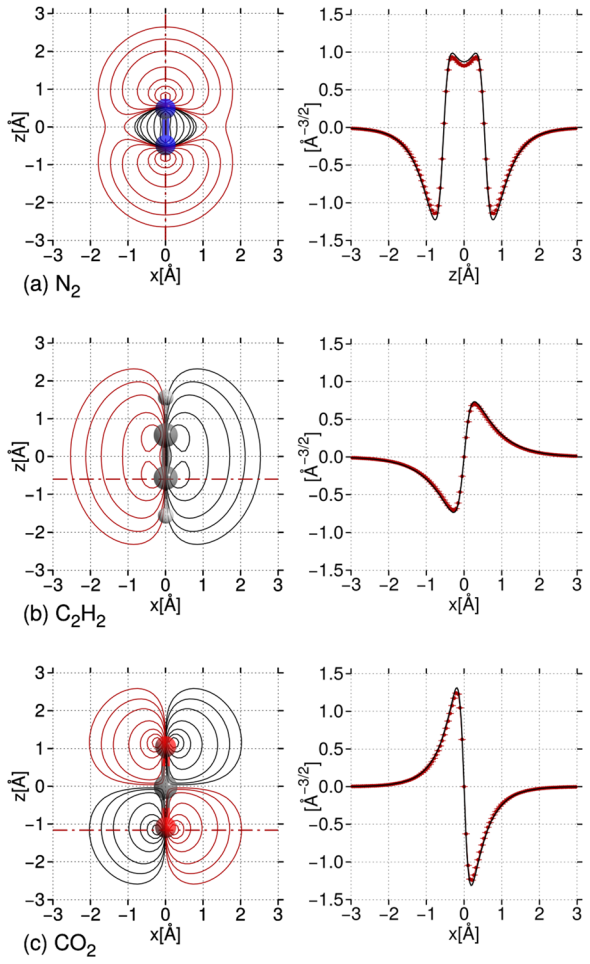

FIG. 2. Left column: contour plots of the *h*QPWFs of (a) N_2, (b) C_2H_2, and (c) CO_2 molecules. Right column: linear plots of the QPWFs (red dots) along the cuts highlighted as red dashed lines in the corresponding right panels, compared with the HOMO obtained from HF calculations (black line) with the same ECP pseudopotential[87] and optimized VTZ basis sets.[88]

DFT (with PBE, PBE0, and B3LYP functionals) are shown in Figs. S1 and S2. In the right panels of Fig. 2, we compare the HF HOMOs with the *h*QPWFs along the axis drawn in red in the corresponding contour plots shown in the left panels. For the π orbitals of the CO_2 and C_2H_2 molecules, the linear plots are presented along the axis orthogonal to the molecular one and passing through the O and C atoms, respectively. For the σ orbital of N_2, we have compared the orbitals along the molecular axis.

For all the three molecules, it is evident that the correlated *h*QPWF does not differ significantly from the single particle picture of the HF HOMO, only a small remodulation of the amplitude being visible. Interestingly, the profile of the N_2 molecule does not correspond to that reported in a previous experimental and computational investigation on the reconstruction of molecular orbitals through HHG tomography.[63]

While in the present work all HOMOs obtained through single particle calculations display a double peak in the region between the atomic centers, in HHG tomography, only a single smooth peak occurs.[63] We find that the presence of the double peak depends on the interatomic distance, as shown in Fig. S3, since it disappears when the bond length is decreased by about 0.3 Å. At the equilibrium geometry, the occurrence of the double peak is confirmed at different levels of theory (Figs. S1–S3), whereas it is absent in the *ab initio* calculations of Ref. 63. On the other hand, the fact that the experimental reconstruction misses these details is not surprising since these are differences visible only for large values of the photoelectron energy, where the signal is low.

This is seen most clearly in the *h*QPWFs built in momentum space through the quantum Monte Carlo procedure described in Sec. II B (Fig. 3). In the left column of Fig. 3, we present the maps of $|\tilde{\varphi}_{h\mathrm{QPWF}}(\mathbf{k})|$ in the two-dimensional space whose axes are the angle Θ between the photoelectron momentum and the molecular axis and the photoelectron energy ϵ_k. Analogous maps obtained by Fourier-transforming the B3LYP and HF HOMOs of the three molecules are reported in Fig. S4. In order to better appreciate the differences between

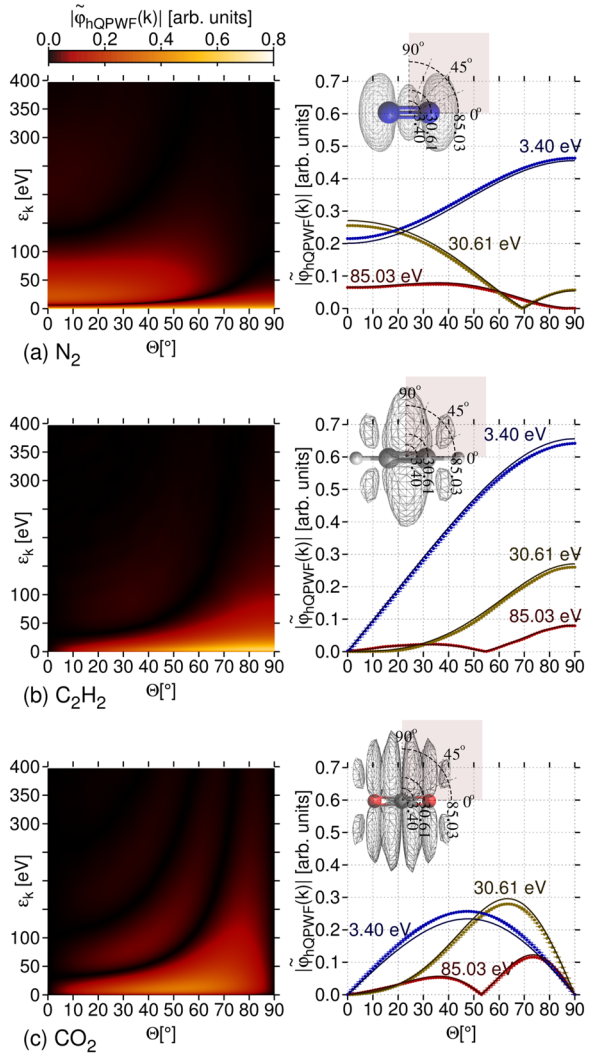

FIG. 3. Left panel: moduli of the *h*QPWF in momentum space for N_2 (a), C_2H_2 (b), and CO_2 (c) along the same planes investigated in Fig. 2. The axes of the contour map are the electron energy $\epsilon_k = \frac{k^2}{2}$ (in atomic units) and the angle Θ between the molecular axis and the photoelectron momentum. Right panel: linear plots of $|\tilde{\varphi}_{h\mathrm{QPWF}}(\mathbf{k})|$ as a function of the angle Θ at selected values of the electron energy (colored dots). These are compared with the corresponding FT of the HF HOMO (solid lines).

the correlated $|\tilde{\varphi}_{h\mathrm{QPWF}}(\mathbf{k})|$ maps and the FT of the HF HOMOs in the right panels of Fig. 3, we compare linear cuts of the maps for selected values of ϵ_k as a function of Θ. We see the largest discrepancies to appear at the smallest energies: the relative amplitudes of both $|\tilde{\varphi}_{h\mathrm{QPWF}}(\mathbf{k})|$ (dots) and HF HOMOs' FT (solid lines) sometimes cross, displaying correlation effects that affect the decay of real-space orbitals. An analogous comparison between $|\tilde{\varphi}_{h\mathrm{QPWF}}(\mathbf{k})|$ and B3LYP HOMO's FT can be found in Fig. S5.

B. Pentacene

After having tested our approach on linear molecules, we address a more complex planar molecular compound previously studied in ARPES experiments.[19] The *h*QPWF in the pentacene molecule, of π symmetry, has already been observed from both ARPES[19] and STS[66] experiments. As above, the first step is to calculate the *h*QPWF through the QMC approach[29] and compare it with single particle HF HOMO (Fig. 4). Also for this conjugated molecule, the difference between the single particle orbital and the *h*QPWF is just a remodulation of the amplitude. In order to understand how this remodulation affects the orbital, the key comparison is between the *h*QPWF in momentum space and the FT of the HF HOMO. In Fig. 5, we simulate the ARPES intensity maps associated with the modulus of the hole quasi-particle wave function ($|\tilde{\varphi}_{h\mathrm{QPWF}}(\mathbf{k})|$) by keeping $|\mathbf{k}| = \sqrt{\frac{2m_e\epsilon_k}{\hbar}}$ fixed. We consider three selected values of the energy ϵ_k of the photoemitted electron increasing from left to right, and we compare these correlated images (bottom row) with those obtained from the FT of HF HOMO (top row). The comparison with the B3LYP HOMO is reported in Fig. S6.

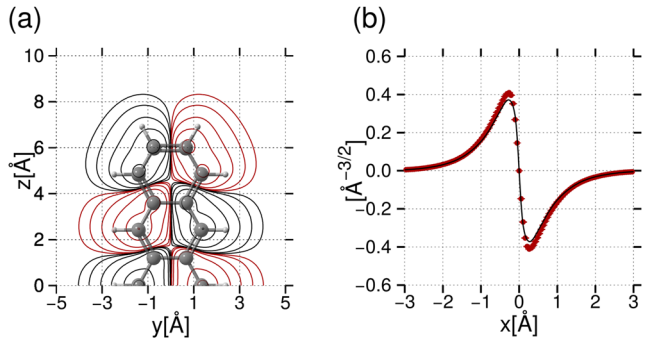

FIG. 4. (a) Contour plot of pentacene's *h*QPWF along a plane parallel to the molecular one at a distance of 0.25 Å. (b) *h*QPWF along the axis perpendicular to the molecular plane and centered on one of the two central carbon atoms (red dots), compared to the HF HOMO (black line).

The symmetry of the plots of Fig. 5 follows from the symmetry of the *h*QPWF in real space. The five peaks that appear along k_z (z being the longitudinal axis of the molecule; see Fig. 1) are symmetric with respect to the origin and are related to three different periodicities that appear in the real *h*QPWF along the same direction.

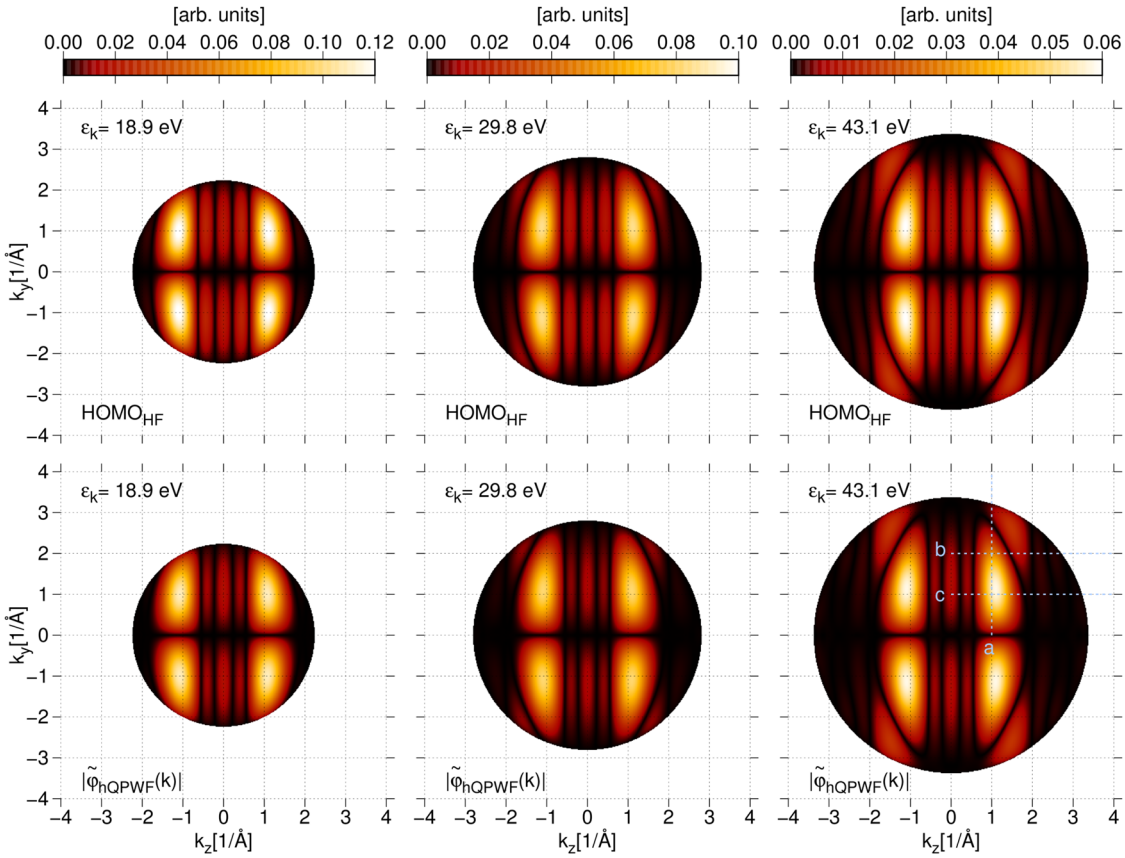

FIG. 5. Top row: Contour plots of the modulus of HF HOMO at fixed energy ϵ_k and wave vector modulus $|\mathbf{k}| = \sqrt{\frac{2m_e\epsilon_k}{\hbar}}$ in the (k_y, k_z) space, for selected values of ϵ_k (increasing from left to right). Bottom row: Contour plots of the corresponding hQPWF, $|\tilde{\varphi}_{h\mathrm{QPWF}}(\mathbf{k})|$. Each plot corresponds to the ARPES detection in the momentum-space hemisphere sketched in Fig. 1.

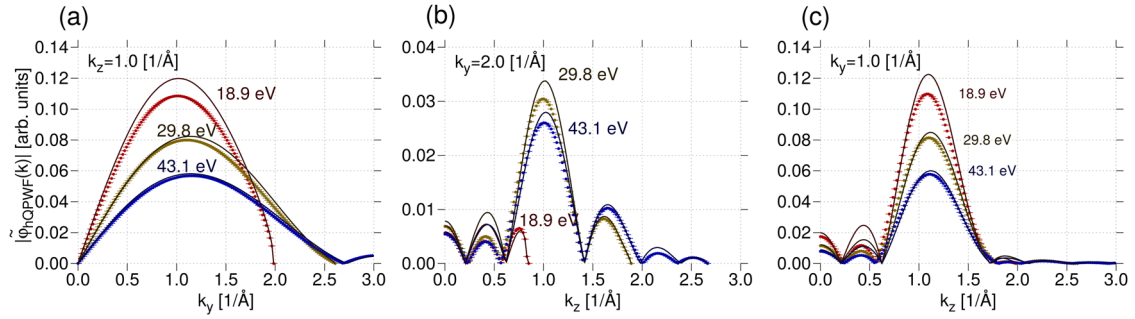

FIG. 6. Comparison between $|\tilde{\varphi}_{h\mathrm{QPWF}}(\mathbf{k})|$ (dots) and the modulus of the HF HOMO's FT (solid lines), corresponding to the same selected energies of the lower right panel of Fig. 5: (a) the k_z component of the momentum is fixed to 1.0 Å^{-1}; (b) the k_y component is 2.0 Å^{-1}; (c) the k_y component is 1.0 Å^{-1}.

Before examining this aspect in depth, we compare in Fig. 5 the heights of $|\tilde{\varphi}_{h\mathrm{QPWF}}(\mathbf{k})|$ and the FT of the HF HOMO. The differences, visible as a partial remodulation of the three central peaks, are better identified through a cut of the amplitudes along selected lines with fixed energy (and thus total momentum $|\mathbf{k}|$) and k_z (or k_y) components. These comparisons are shown in Fig. 6 along three different lines displayed in the bottom right panel of Fig. 5 and labeled accordingly. In panel 6(a), $|\tilde{\varphi}_{h\mathrm{QPWF}}(\mathbf{k})|$ is plotted for three different energies and fixed $k_z = 1.0$ Å^{-1} momentum; in panels 6(b) and 6(c), k_y is fixed to 2.0 Å^{-1} and 1.0 Å^{-1}, respectively. While in the first panel [Fig. 6(a)] only the remodulation of the most intense peak is visible for different photon energies, in panels 6(b) and 6(c), three lower momentum peaks can be identified, which are centered, respectively, at k_z equal to 0.0 Å^{-1}, 0.45 Å^{-1}, and 1.0 Å^{-1} [the last peak corresponds to the one also visible in Fig. 6(a)].

To understand how these three peaks are related to the periodicity of the orbital, we manipulate the FT of the HF HOMO by selectively enhancing one of the three peaks by a factor 2 and preserving the image's symmetry. Afterwards, by doing the reverse FT, we obtain a HOMO affected by these modifications. By subtracting from these images the unmodified HOMO, it is possible to visualize the changes in the amplitudes induced by the manipulation of the FT peaks.

In Fig. 7(a), we show the surface plots of the HF HOMO, and in panels 7(b)–7(d), we show the differences between the modified orbitals and the original HF HOMO, along a plane parallel to the molecular one and at a distance of 0.25 Å. The first modulation in panel 7(b) is related to the enhancing of the first peak centered in $k_z = 0.0$ Å^{-1}, the second one [panel 7(c)] is related to the changing of the second peak centered in $k_z = 0.45$ Å^{-1}, and the last one [panel 7(d)] is related to the peak centered approximately at $k_y = k_z = 1.0$ Å^{-1}. A better understanding of the modulations can be achieved by comparing them together with the HF HOMO [Fig. 8(b)] along a chosen cut of the previous plane [dotted line in Fig. 8(a)]. The cosine-like modulation that comes from the first peak [panel 7(b) and labeled as (1) in Fig. 8(b)] has a periodicity equal to the extension of the orbital. The enhancement of this peak leads to an increase in the HOMO's amplitude in the positive regions and to a decrease in the negative ones. The middle peak is related to a second order periodicity that displaces the charge distribution of the orbital from the center towards the edge [labeled as (2) in Fig. 8(b)]. The third peak is related to a modulation that has approximately the same nodal structure and sign of the real space orbital; thus, its absolute value increases monotonously with the modulation [labeled as (3) in Fig. 8(b)].

Overall, we are able to pinpoint which real-space feature depends on a specific FT peak. In particular, since the 1.0 Å^{-1}

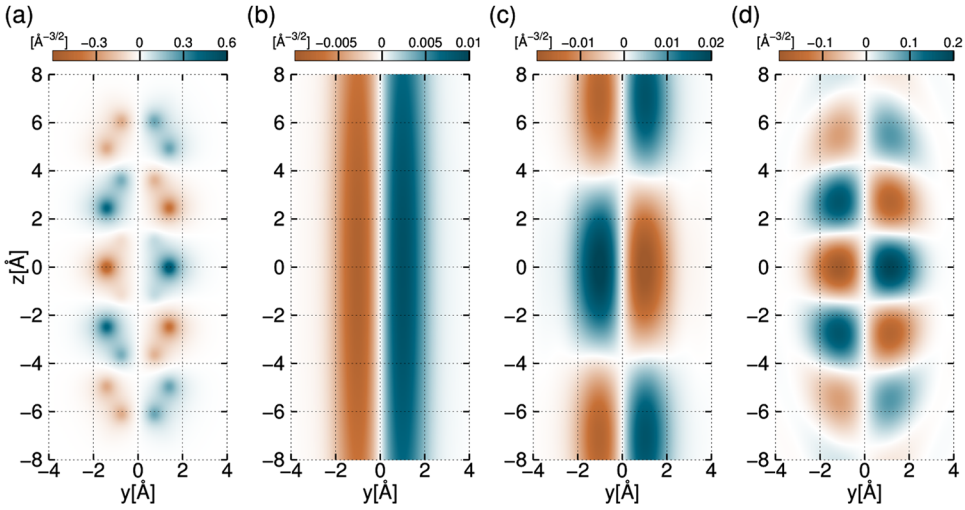

FIG. 7. Surface plots parallel to the molecular plane at a distance of 0.25 Å: (a) the HOMO orbital of pentacene obtained from HF. (b) Difference between the HOMO orbital and the modified one obtained by enhancing the series of first peaks in the FT ($k_y = 1$ Å^{-1}, $k_z = 0$ Å^{-1}, and the symmetric ones). (c) Difference between the HOMO orbital and that obtained by enhancing the series of second peaks in the FT ($|k_y| = 1$ Å^{-1}, $|k_z| = 0.5$ Å^{-1}). (d) Difference between the HOMO orbital and that obtained by enhancing the series of third peaks in the FT ($|k_y| = 1$ Å^{-1}, $|k_z| = 1.0$ Å^{-1}).

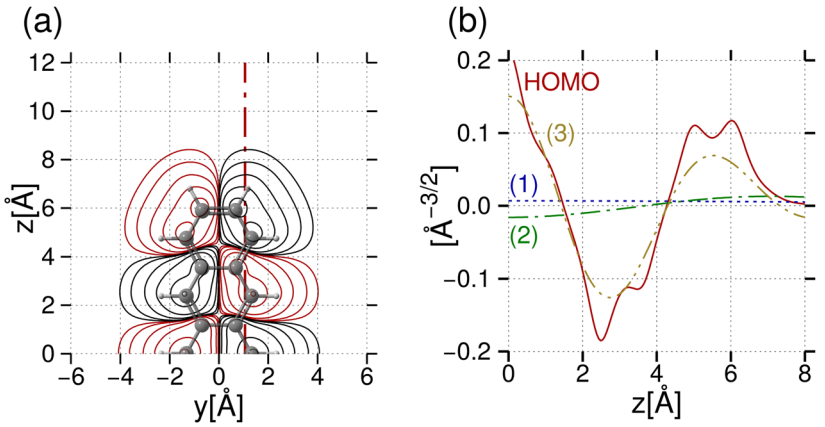

FIG. 8. (a) Contour plot of the HF HOMO of pentacene along a plane parallel to the molecular one, at a distance of 0.25 Å. (b) Cut of the HF HOMO orbital along the red dotted line of panel (a), together with the three modulations defined as the differences between the HOMO orbital and the FT of the momentum space image in which we enhance by a factor 2.0 the three peaks shown in panel 6(a).

peak of the $|\tilde{\varphi}_{h\mathrm{QPWF}}(\mathbf{k})|$ is lower than that of the HF HOMO's FT, the amplitude of the real space *h*QPWF is lower than that of the HF HOMO, as expected by the fact that the *h*QPWF's norm is ≤ 1 due to correlation effects. Second, since the 0.45 Å^{-1} peak in the $|\tilde{\varphi}_{h\mathrm{QPWF}}(\mathbf{k})|$ is lower than that of the HF HOMO's FT, we can deduce that along the longitudinal direction, the *h*QPWF is more localized in the center with respect to the HF HOMO. We also notice that this FT-to-real space analysis may be useful for the interpretation of the experimental results as well.

C. $CuCl_4^{2-}$ planar complex

As the last system, we consider the planar $CuCl_4^{2-}$ complex, of which the *h*QPWF has been previously calculated by us in Ref. 29. In this metallic compound, we were able to identify correlation effects beyond the single particle picture, especially in the absorption process, related to the modulus of the *e*QPWF, i.e., the probability density of adding an electron to the reference state. Here we want to trace correlation effects in the photodissociation process; thus, we compute the $|\tilde{\varphi}_{h\mathrm{QPWF}}(\mathbf{k})|$ in momentum space for three fixed values of the

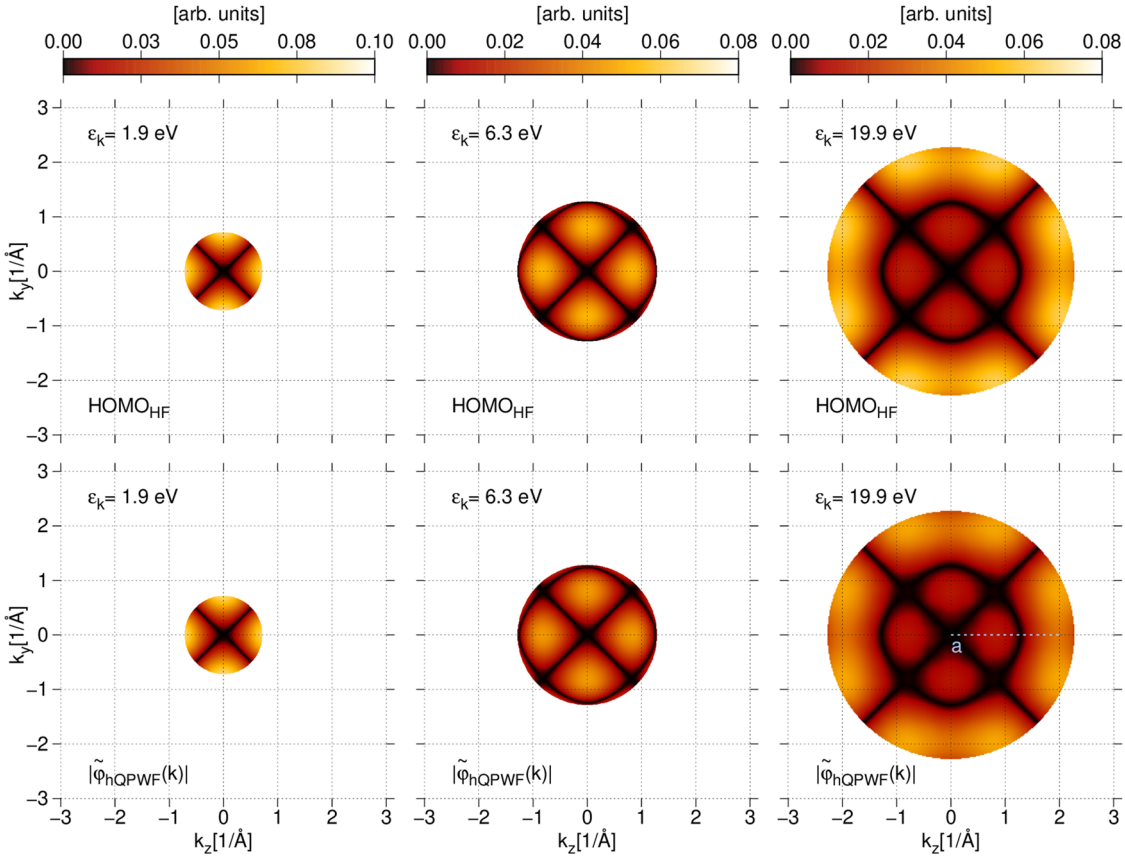

FIG. 9. The planar $CuCl_4^{2-}$ complex. Top row: Contour plots of the modulus of HF HOMO-1 at fixed energy ϵ_k and wave vector modulus $|\mathbf{k}| = \sqrt{\frac{2m_e\epsilon_k}{\hbar}}$ in the (k_y, k_z) space, for selected values of ϵ_k (increasing from left to right). Bottom row: Contour plots of the corresponding hQPWF, $|\tilde{\varphi}_{h\mathrm{QPWF}}(\mathbf{k})|$. Each plot corresponds to the ARPES detection in the momentum-space hemisphere.

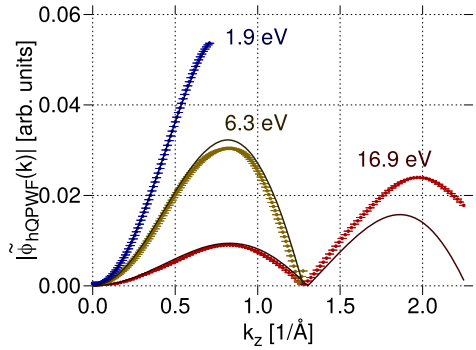

FIG. 10. Effect of correlations in $CuCl_4^{2-}$. Comparison between $|\tilde{\varphi}_{h\mathrm{QPWF}}(\mathbf{k})|$ (dots) and the modulus of the HF HOMO-1's FT (solid lines), corresponding to the same selected energies of Fig. 9.

photoelectron energy, obtaining the three hemispheres plotted in the lower panels of Fig. 9 along the molecular plane. These values are compared with the FT of the HF HOMO-1 reported in the top panels of Fig. 9 (the comparison with the B3LYP single particle orbitals is reported in Fig. S8 of the supplementary material). We must point out that in our unrestricted DFT and HF calculations, the correct orbital to compare with the *h*QPWF is the HOMO-1 due to an erroneous ordering of the orbital eigenvalues.[29] By comparing the $|\tilde{\varphi}_{h\mathrm{QPWF}}(\mathbf{k})|$ signal and the FT of the HF HOMO-1, it becomes clear that as the photoelectron energy increases, the intensity of the $|\tilde{\varphi}_{h\mathrm{QPWF}}(\mathbf{k})|$ becomes more intense with respect to that of the FT HOMO-1. To better distinguish the differences between the two in Fig. 10, we compare them along the cut shown on the bottom right panel of Fig. 9. From these linear plots, it is clear that the increase of the photoelectron energy, that corresponds to smaller length scales in the molecular orbital, reveals substantial differences between $|\tilde{\varphi}_{h\mathrm{QPWF}}(\mathbf{k})|$ and FT of the HF HOMO-1 as shown in Ref. 29. These correlation effects, although attenuated, are also visible when comparing the $|\tilde{\varphi}_{h\mathrm{QPWF}}(\mathbf{k})|$ and FT of the B3LYP HOMO-1 (the differences are shown in Fig. S9 of the supplementary material).

V. CONCLUSIONS

In this work, we have proposed a procedure based on QMC to straightforwardly compute the quasiparticle wave functions in momentum space, whose square modulus corresponds to the ARPES map, in a plane-wave approximation. Different from the Fourier transform of single particle molecular orbitals, usually used to interpret ARPES experiments, the QPWFs include correlation effects between the electron that is photoemitted and the other electrons in the molecule, being dressed by few-body interactions. This procedure has been applied to the correlated Jastrow antisymmetrized geminal power (JAGP) wave function, which is essentially a multideterminantal expansion that includes the correlation between the electronic variables through explicit few-body terms. This procedure might be advantageous for large molecular systems that also require the inclusion of static electronic correlations due to partial orbital degeneracy like, for example, transition metal compounds or multiradicals. As a matter of fact, despite the overall computational prefactor, the QMC algorithms are highly parallelizable and scale at most as the fourth power of the number of electrons in the system, making them extremely efficient in the modern computing facilities. Furthermore, it is possible to integrate, and thus to optimize, multideterminantal trial wave functions also including explicit few-body interactions through the Jastrow factors. To test our QMC procedure, we have first calculated the photoemitted electron energy map, of three linear molecules, as a function of the inclination angle between the electron's momentum and the molecular axis. For these results, only small differences could be seen between the correlated *h*QPWF and the FT of the HF HOMO. The small remodulations of the FT peaks with respect to the *h*QPWF in momentum space were associated with the lack of spectral weight of the *h*QPWF in real space, as compared to the HF molecular orbital.

Afterwards, we have studied the ARPES map of pentacene, which has already been the object of different orbital reconstruction experiments. By comparing our momentum space *h*QPWF with the FT of the HF HOMO, we have clearly identified different remodulations of the orbital peaks that in real space correspond to the relocation of the charge along the electronic orbital (beyond the overall spectral weight renormalization). The correlated *h*QPWF in real space was found to be more localized close the center of the molecule with respect to the corresponding HF HOMO.

Finally we have studied the $CuCl_4^{2-}$ planar complex in which we have shown the erroneous ordering of the frontier orbitals predicted by the unrestricted single particle calculations and we were able to distinguish short range correlation effects with respect to the Hartree-Fock reference; admittedly smaller differences (although still not negligible) were found comparing with B3LYP DFT results.

In conclusion, the QMC approach that we have presented to compute the QPWFs in momentum space, calculating the photoemission transition probabilities measured in ARPES experiments, has revealed correlation effects that go beyond the single particle representation typically used to interpret the experiments. The QPWF in momentum space is more sensitive than the real space image and can reveal correlation effects that affect the real space orbitals. We hope that these results will stimulate further experimental and computational investigations to characterize more complex molecular compounds and their electronic properties. We also envision that recent advances in QMC methods will enable the study of photoemission processes involving deeper occupied electronic orbitals with the use of excited states calculations.[89–92]

SUPPLEMENTARY MATERIAL

See supplementary material for tests on basis set convergence on energy and the role of pseudopotential and additional comparison of quasiparticle wave functions with B3LYP orbitals.

ACKNOWLEDGMENTS

M.B., M.R., and S.C. acknowledge funds from the PRIN 2012 Project *MEMO—"Imaging MEtallorganic MOlecules:*

Scanning tunneling spectroscopy and many-body theory." Computational resources have been granted by the CINECA HPC center through the ISCRA B project IscrB_STSQMC.

[1] A. Damascelli, Z. Hussain, and Z.-X. Shen, Rev. Mod. Phys. **75**, 473 (2003).
[2] P. Puschnig, S. Berkebile, A. J. Fleming, G. Koller, K. Emtsev, T. Seyller, J. D. Riley, C. Ambrosch-Draxl, F. P. Netzer, and M. G. Ramsey, Science **326**, 702 (2009).
[3] A. Perveaux, D. Lauvergnat, B. Lasorne, F. Gatti, M. A. Robb, G. J. Halasz, and A. Vibok, J. Phys. B: At., Mol. Opt. Phys. **47**, 124010 (2014).
[4] P. Salières, A. Maquet, S. Haessler, J. Caillat, and R. Taïeb, Rep. Prog. Phys. **75**, 062401 (2012).
[5] A. Crawford-Uranga, U. D. Giovannini, D. J. Mowbray, S. Kurth, and A. Rubio, J. Phys. B: At., Mol. Opt. Phys. **47**, 124018 (2014).
[6] S. Hagen, Y. Luo, R. Haag, M. Wolf, and P. Tegeder, New J. Phys. **12**, 125022 (2010).
[7] Z. Liu, Y. Chen, J. Analytis, S. Mo, D. Lu, R. Moore, I. Fisher, Z. Hussain, and Z. Shen, Physica E **44**, 891 (2012).
[8] P. Puschnig, E.-M. Reinisch, T. Ules, G. Koller, S. Soubatch, M. Ostler, L. Romaner, F. S. Tautz, C. Ambrosch-Draxl, and M. G. Ramsey, Phys. Rev. B **84**, 235427 (2011).
[9] F. Himpsel, J. Electron Spectrosc. Relat. Phenom. **183**, 114 (2011).
[10] S. Berkebile, T. Ules, P. Puschnig, L. Romaner, G. Koller, A. J. Fleming, K. Emtsev, T. Seyller, C. Ambrosch-Draxl, F. P. Netzer, and M. G. Ramsey, Phys. Chem. Chem. Phys. **13**, 3604 (2011).
[11] H. Liu, S.-F. Zhao, M. Li, Y. Deng, C. Wu, X.-X. Zhou, Q. Gong, and Y. Liu, Phys. Rev. A **88**, 061401 (2013).
[12] D. Lüftner, M. Milko, S. Huppmann, M. Scholz, N. Ngyuen, M. Wiener, A. Schöll, F. Reinert, and P. Puschnig, J. Electron Spectrosc. Relat. Phenom. **195**, 293 (2014).
[13] Y. Liu, D. Ikeda, S. Nagamatsu, T. Nishi, N. Ueno, and S. Kera, J. Electron Spectrosc. Relat. Phenom. **195**, 287 (2014).
[14] C. S. Fadley and S. Nemk, J. Electron Spectrosc. Relat. Phenom. **195**, 409 (2014).
[15] S. Cohen, M. M. Harb, A. Ollagnier, F. Robicheaux, M. J. J. Vrakking, T. Barillot, F. Lépine, and C. Bordas, Phys. Rev. Lett. **110**, 183001 (2013).
[16] H. Offenbacher, D. Lüftner, T. Ules, E. M. Reinisch, G. Koller, P. Puschnig, and M. G. Ramsey, J. Electron Spectrosc. Relat. Phenom. **204**, 92 (2015).
[17] V. Feyer, M. Graus, P. Nigge, G. Zamborlini, R. Acres, A. Schöll, F. Reinert, and C. Schneider, J. Electron Spectrosc. Relat. Phenom. **204**, 125 (2015).
[18] C. Miron, C. Nicolas, O. Travnikova, P. Morin, Y. Sun, F. Gel'mukhanov, N. Kosugi, and V. Kimberg, Nat. Phys. **8**, 135 (2012).
[19] D. Lüftner, T. Ules, E. M. Reinisch, G. Koller, S. Soubatch, F. S. Tautz, M. G. Ramsey, and P. Puschnig, Proc. Natl. Acad. Sci. U. S. A. **111**, 605 (2014).
[20] M. Dauth, M. Wiessner, V. Feyer, A. Schöll, P. Puschnig, F. Reinert, and S. Kümmel, New J. Phys. **16**, 103005 (2014).
[21] M. Waitz, R. Y. Bello, D. Metz, J. Lower, F. Trinter, C. Schober, M. Keiling, U. Lenz, M. Pitzer, K. Mertens, M. Martins, J. Viefhaus, S. Klumpp, T. Weber, L. P. H. Schmidt, J. B. Williams, M. S. Schöffler, V. V. Serov, A. S. Kheifets, L. Argenti, A. Palacios, F. Martìn, T. Jahnke, and R. Dörner, Nat. Commun. **8**, 2266 (2017).
[22] A. M. Bradshaw and D. P. Woodruff, New J. Phys. **17**, 013033 (2015).
[23] P. Puschnig and D. Lüftner, J. Electron Spectrosc. Relat. Phenom. **200**, 193 (2015).
[24] B. Barbiellini and A. Bansil, J. Phys. Chem. Solids **65**, 2031 (2004).
[25] C. Melania Oana and A. I. Krylov, J. Chem. Phys. **127**, 234106 (2007).
[26] D. Toroz, M. Rontani, and S. Corni, J. Chem. Phys. **134**, 024104 (2011).
[27] D. Toroz, M. Rontani, and S. Corni, Phys. Rev. Lett. **110**, 018305 (2013).
[28] F. Schulz, M. Ijas, R. Drost, S. K. Hamalainen, A. Harju, A. P. Seitsonen, and P. Liljeroth, Nat. Phys. **11**, 229 (2015).
[29] M. Barborini, S. Sorella, M. Rontani, and S. Corni, J. Chem. Theory Comput. **12**, 5339 (2016).
[30] N. L. Nguyen, G. Borghi, A. Ferretti, I. Dabo, and N. Marzari, Phys. Rev. Lett. **114**, 166405 (2015).
[31] S. Weisz, D. Lüftner, T. Ules, E. M. Reinisch, H. Kaser, A. Gottwald, M. Richter, S. Soubatch, G. Koller, M. G. Ramsey, F. S. Tautz, and P. Puschnig, Nat. Commun. **6**, 8287 (2015).
[32] M. Dauth and S. Kümmel, Phys. Rev. A **93**, 022502 (2016).
[33] L. Kronik and S. Kümmel, "Gas-phase valence-electron photoemission spectroscopy using density functional theory," in *First Principles Approaches to Spectroscopic Properties of Complex Materials* (Springer, Berlin, 2014), pp. 137–191.
[34] M. Wießner, D. Hauschild, C. Sauer, A. Feyer, V. amd Schöll, and F. Reinert, Nat. Commun. **5**, 4156 (2014).
[35] J. Ziroff, F. Forster, A. Schöll, P. Puschnig, and F. Reinert, Phys. Rev. Lett. **104**, 233004 (2010).
[36] M. Wießner, J. Ziroff, F. Forster, M. Arita, K. Shimada, P. Puschnig, A. Schöll, and F. Reinert, Nat. Commun. **4**, 1514 (2013).
[37] U. De Giovannini, D. Varsano, M. A. L. Marques, H. Appel, E. K. U. Gross, and A. Rubio, Phys. Rev. A **85**, 062515 (2012).
[38] M. Dauth, M. Graus, I. Schelter, M. Wießner, A. Schöll, F. Reinert, and S. Kümmel, Phys. Rev. Lett. **117**, 183001 (2016).
[39] S. Gozem, A. O. Gunina, T. Ichino, D. L. Osborn, J. F. Stanton, and A. I. Krylov, J. Phys. Chem. Lett. **6**, 4532 (2015).
[40] R. Gaillac, M. Vacher, A. Maquet, R. Taïeb, and J. Caillat, Phys. Rev. A **93**, 013410 (2016).
[41] C. Zhai, L. He, P. Lan, X. Zhu, Y. Li, F. Wang, W. Shi, Q. Zhang, and P. Lu, Sci. Rep. **6**, 23236 (2016).
[42] P. Puschnig, A. D. Boese, M. Willenbockel, M. Meyer, D. Lftner, E. M. Reinisch, T. Ules, G. Koller, S. Soubatch, M. G. Ramsey, and F. S. Tautz, J. Phys. Chem. Lett. **8**, 208 (2017).
[43] J. P. Perdew and A. Zunger, Phys. Rev. B **23**, 5048 (1981).
[44] D. P. Chong, O. V. Gritsenko, and E. J. Baerends, J. Chem. Phys. **116**, 1760 (2002).
[45] M. Dauth, T. Körzdörfer, S. Kümmel, J. Ziroff, M. Wiessner, A. Schöll, F. Reinert, M. Arita, and K. Shimada, Phys. Rev. Lett. **107**, 193002 (2011).
[46] N. Dori, M. Menon, L. Kilian, M. Sokolowski, L. Kronik, and E. Umbach, Phys. Rev. B **73**, 195208 (2006).
[47] T. Stein, H. Eisenberg, L. Kronik, and R. Baer, Phys. Rev. Lett. **105**, 266802 (2010).
[48] T. Körzdörfer and S. Kümmel, Phys. Rev. B **82**, 155206 (2010).
[49] L. Kronik, T. Stein, S. Refaely-Abramson, and R. Baer, J. Chem. Theory Comput. **8**, 1515 (2012).
[50] S. Refaely-Abramson, S. Sharifzadeh, N. Govind, J. Autschbach, J. B. Neaton, R. Baer, and L. Kronik, Phys. Rev. Lett. **109**, 226405 (2012).
[51] W. M. C. Foulkes, L. Mitas, R. J. Needs, and G. Rajagopal, Rev. Mod. Phys. **73**, 33 (2001).
[52] J. Kolorenč and L. Mitas, Rep. Prog. Phys. **74**, 026502 (2011).
[53] B. M. Austin, D. Y. Zubarev, and W. A. Lester, Chem. Rev. **112**, 263 (2012).
[54] N. D. Drummond, M. D. Towler, and R. J. Needs, Phys. Rev. B **70**, 235119 (2004).
[55] M. Marchi, S. Azadi, C. Casula, and S. Sorella, J. Chem. Phys. **131**, 154116 (2009).
[56] S. Sorella, Phys. Rev. Lett. **64**, 24512 (2001).
[57] S. Sorella, Phys. Rev. B **71**, 241103 (2005).
[58] C. J. Umrigar, J. Toulouse, C. Filippi, S. Sorella, and R. G. Hennig, Phys. Rev. Lett. **98**, 110201 (2007).
[59] S. Sorella and S. Capriotti, J. Chem. Phys. **133**, 234111 (2010).
[60] M. Barborini, S. Sorella, and L. Guidoni, J. Chem. Theory Comput. **8**, 1260 (2012).
[61] A. Zen, Y. Luo, G. Mazzola, L. Guidoni, and S. Sorella, J. Chem. Phys. **142**, 144111 (2015).
[62] S. Saccani, C. Filippi, and S. Moroni, J. Chem. Phys. **138**, 084109 (2013).
[63] J. Itatani, J. Levesque, D. Zeidler, H. Niikura, H. Pepin, J. C. Kieffer, P. B. Corkum, and D. M. Villeneuve, Nature **432**, 867 (2004).
[64] O. Smirnova, Y. Mairesse, S. Patchkovskii, N. Dudovich, D. Villeneuve, P. Corkum, and M. Y. Ivanov, Nature **460**, 972 (2009).
[65] C. Vozzi, M. Negro, F. Calegari, G. Sansone, M. Misoli, S. De Silvestri, and S. Stagira, Nat. Phys. **7**, 822 (2011).
[66] J. Repp, G. Meyer, S. M. Stojković, A. Gourdon, and C. Joachim, Phys. Rev. Lett. **94**, 026803 (2005).
[67] M. Casula and S. Sorella, J. Chem. Phys. **119**, 6500 (2003).
[68] M. Casula, C. Attaccalite, and S. Sorella, J. Chem. Phys. **121**, 7110 (2004).
[69] M. Marchi, S. Azadi, and S. Sorella, Phys. Rev. Lett. **107**, 086807 (2011).
[70] S. Sorella, M. Casula, and D. Rocca, J. Chem. Phys. **127**, 014105 (2007).
[71] M. Barborini and L. Guidoni, J. Chem. Phys. **137**, 224309 (2012).
[72] A. Zen, E. Coccia, Y. Luo, S. Sorella, and L. Guidoni, J. Chem. Theory Comput. **10**, 1048 (2014).
[73] M. Barborini and L. Guidoni, J. Chem. Theory Comput. **11**, 508 (2015).
[74] A. Zen, E. Coccia, S. Gozem, M. Olivucci, and L. Guidoni, J. Chem. Theory Comput. **11**, 992 (2015).
[75] M. Barborini and L. Guidoni, J. Chem. Theory Comput. **11**, 4109 (2015).
[76] J. A. Pople, Proc. R. Soc. A **202**, 323 (1950).
[77] A. J. Coleman, Rev. Mod. Phys. **35**, 668 (1963).
[78] A. J. Coleman, J. Math. Phys. **6**, 1425 (1965).
[79] M. Casalegno, M. Mella, and A. M. Rappe, J. Chem. Phys. **118**, 7193 (2003).

[80]F. Sterpone, L. Spanu, L. Ferraro, S. Sorella, and L. Guidoni, J. Chem. Theory Comput. **4**, 1428 (2008).
[81]S. Sorella, "TurboRVB quantum Monte Carlo package" (accessed 21 May 2015).
[82]F. Neese, Wiley Interdiscip. Rev.: Comput. Mol. Sci. **2**, 73 (2012).
[83]G. Herzberg, *Electronic Spectra and Electronic Structure of Polyatomic Molecules* (Van Nostrand, New York, 1966).
[84]K. Kuchitsu, *Structure of Free Polyatomic Molecules: Basic Data* (Springer, Berlin, 1998).
[85]K. P. Huber and G. Herzberg, *Molecular Spectra and Molecular Structure. IV. Constants of Diatomic Molecules* (Van Nostrand Reinhold Co., 1979).
[86]T. H. Dunning, J. Chem. Phys. **90**, 1007 (1989).
[87]M. Burkatzki, C. Filippi, and M. Dolg, J. Chem. Phys. **126**, 234105 (2007).
[88]M. Burkatzki, C. Filippi, and M. Dolg, "Energy-consistent pseudopotentials for QMC calculations" (accessed 6 June 2015).
[89]O. Valsson, C. Angeli, and C. Filippi, Phys. Chem. Chem. Phys. **14**, 11015 (2012).
[90]F. Schautz and C. Filippi, J. Chem. Phys. **120**, 10931 (2004).
[91]O. E. Akramine, A. C. Kollias, and J. W. A. Lester, J. Chem. Phys. **119**, 1483 (2003).
[92]H. Zulfikri, C. Amovilli, and C. Filippi, J. Chem. Theory Comput. **12**, 1157 (2016).